ISBN: 978-981-18-5852-9
WCSE 2022 Spring Event: 2022 9th International Conference on Industrial Engineering and Applications
doi: 10.18178/wcse.2022.04.118

Scattering of Stealth-material Objects Illuminated by OAM Beams

Zhong Yu [1], Bingwen He[1+] and Pan Wang[1]

[1] School of Information and Communication Engineering, Xi'an University of Posts & Telecommunications, Xi'an, China

Abstract. The high-order Bessel vortex beam (BVB) carrying orbital angular momentum (OAM) is used to study the scattering characteristics of the stealth-material (SM) triangular pyramid and the SM cube for evaluating the interaction between the orbital angular momentum (OAM) beams and the SM standard objects. We use the radial point interpolation method (RPIM) algorithm to calculate the electric and magnetic field values which are used in the near-field to far-field transformation (NFFFT), and use the RCS empirical formula to calculate the value of the RCS. The results show that the RCS increases obviously when the BVB beam illuminate the target objects. Then, the scattering field is calculated for analyzing the phase distribution and OAM spectrum in detail. The results show that the scattering field of axisymmetric objects still retains the main characteristics of vortex field due to the conservation of angular momentum. Therefore, compared with plane waves, OAM beams possess more potential for anti-stealth target detection and recognition.

Keywords: anti-stealth, orbital angular momentum (OAM), radar cross section (RCS), scattering, stealth-material (SM).

1. Introduction (Use "Header 1" Style)

Radar emits electromagnetic waves to illuminate the targets, and receives the reflected electromagnetic waves to detect and image it. With the development of stealth-material (SM) technology, the smaller Radar Cross Section (RCS) of the target make detection of stealthy targets more difficult [1-4]. At present, radar anti-stealth technology is principally divided into frequency domain anti-stealth, such as ultra-wideband radar (Airspace anti stealth)[5], multi-base radar (polarization domain anti-stealth)[6, 7], polarization radar, etc. Recently, a new radar scheme based on Orbital Angular Momentum (OAM) has been proposed. It focuses on using OAM beam to carry out structural anti-stealth in the aspect of anti-stealth in OAM domain[8]. However, there are few researches on anti-stealth techniques using OAM scattering characteristics.

Electromagnetic (EM) waves carrying OAM have helical wave fronts with different topological charges, which leads to rich scattering phenomena. In literature[9], the scattering of a high-order Bessel beam by a sphere is reported. Yu et al. investigate the scattering of non-diffracting high-order Bessel vortex beam (BVB) by radar targets[10]. The effects by OAM intrinsic mode characteristics on the radar scattering cross section are studied. Wu et al. use the series expansion and the physical optics (PO) methods to calculate scattering field[11]. The scattering field is simulated and measured, and the results effectively explain the interaction between OAM wave and metal target sphere. In [12], the scattering characteristics of a metal flat plate illuminating by vortex EM waves are investigated. Then, the scattering field of OAM wave and plane wave are compared. Liu et al. study the backward scattering characteristics of perfect electrical conductor (PEC) sphere and PEC cone to evaluate the interaction between the OAM beams and the electrically-large standard objects[13]. Some unique characters of the OAM scattering have been found in the literatures above. However, the scattering characteristics of the SM objects illuminated by OAM beams has not been studied yet.

This paper is outlined as follows. Section II presents the radial point interpolation method (RPIM) algorithm to calculate the electric and magnetic field values, which are used in the near-field to far-field transformation (NFFFT) method, and used the RCS empirical formula to calculate the value of RCS. In

[+] Corresponding author.
E-mail address: hbw991499@163.com.

addition, the essential formulations of the BVB are presented. The numerical results of this work are presented in Section III. The conclusion is stated in Section IV.

2. Method

Bessel beam is a typical non-diffraction beam. When Helmholtz equation is solved in cylindrical coordinate system, the cube illuminated by Bessel beam can be obtained in Fig 1, which can be expressed as

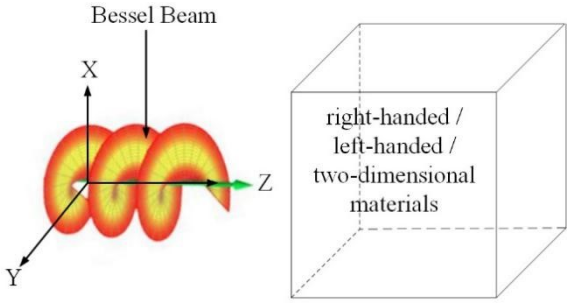

Fig. 1: The Schematic diagram of a stealth material cube illuminated by Bessel vortex wave.

$$\begin{Bmatrix} E_x \\ E_y \\ E_z \end{Bmatrix} = E_S e^{ik(z-z_0)} \begin{Bmatrix} i^l J_l(\sigma_m)e^{il\phi_m} - (1/2)P_\perp \begin{bmatrix} i^{l+2}J_{l+2}(\sigma_m)e^{i(l+2)\phi_m} \\ i^{l-2}J_{l-2}(\sigma_m)e^{i(l-2)\phi_m} \end{bmatrix} \\ -(1/2i)P_\perp \begin{bmatrix} i^{l+2}J_{l+2}(\sigma_m)e^{i(l+2)\phi_m} \\ i^{l-2}J_{l-2}(\sigma_m)e^{i(l-2)\phi_m} \end{bmatrix} \\ -P_\parallel \left[i^{l+1} I_{l+1}(\sigma_m)e^{i(l+1)\phi_m} + i^{l-1}J_{l-1}(\sigma_m)e^{i(l-1)\phi_m} \right] \end{Bmatrix} \tag{1}$$

where, J(•) is the Bessel function of first kind.

$$\phi_m = \arctan\left[(y-y_0)/(x-x_0)\right], \sigma_m = k_p \rho_m \sin(\alpha_0) \tag{2}$$

$$\rho_m = \sqrt{(x-x_0)^2+(y-y_0)^2}, p_\perp = (1-\cos\alpha_0)/(1+\cos\alpha_0) \tag{3}$$

$$p_\parallel = (\sin\alpha_0)/(1+\cos\alpha_0), E_S = \pi E_{pw}(1+\cos\alpha_0) \tag{4}$$

where Φm is azimuthal coordinates in the transverse plane，σm is the electrical conductivity of the electric field component, kp is wave number, and ρm is the charge density of the electric field. Where $p_\parallel$ is the power density parallel to the electric field vector, and $p_\perp$ the power density perpendicular to the electric field vector.

The Bessel vortex beam (BVB) is a typical vortex electromagnetic wave, which has the characteristics of non-diffraction propagation, small central spot diameter, good directionality and long propagation distance, etc., and has been widely used in electromagnetic research.

We use the Radial Point Interpolation Method (RPIM) [11] to calculate the near-field electromagnetic values. The RPIM adopt the radial basis function Bi(x) and polynomial basis function Pj(x). The approximate function evaluated at the node xi inside support domain is assumed to be ui [14].

$$u(\boldsymbol{x}) = \sum_{i=1}^{n} B_i(\boldsymbol{x})a_i + \sum_{j=1}^{m} P_j(\boldsymbol{x})b_j = \boldsymbol{B}^T(\boldsymbol{x})\boldsymbol{a} + \boldsymbol{P}^T(\boldsymbol{x})\boldsymbol{b} \tag{5}$$

Where, ai, bj are the coefficients for Bi(x) and Pj(x), respectively. The n is the number of scatter nodes in support domain x, m is the number of polynomial basis function. Then, the Maxwell equation is used to update the near-field electromagnetic values.

The NFFFT [15] method is used to gain the far-field electromagnetic values. It is necessary to adopt the empirical formula to calculate the value of RCS. The domain is excited with a total-field/scattered-field (TF/SF) scheme based on the RPIM method and truncated by means of a perfectly matched layer (PML). To acquire the bistatic RCS of the stealth-material (SM) section, a near-to-far field transformation is applied at the rectangular surface S in the scattered field region. Far-field field components at distance r, are obtained in term of [16]

$$E_\theta(\boldsymbol{r},t) = -\eta_0 W_\theta(\boldsymbol{r},t) - U_\varphi(\boldsymbol{r},t) \tag{6}$$

$$E_\varphi(\boldsymbol{r},t) = -\eta_0 W_\varphi(\boldsymbol{r},t) + U_\theta(\boldsymbol{r},t) \tag{7}$$

where

$$\boldsymbol{W}(\boldsymbol{r},t) = \frac{1}{4\pi rc}\frac{\partial}{\partial t}[\iint_S J_S(t - \frac{r - \boldsymbol{r}'\cdot\hat{\boldsymbol{r}}}{c})dS'] \tag{8}$$

$$\boldsymbol{U}(\boldsymbol{r},t) = \frac{1}{4\pi rc}\frac{\partial}{\partial t}[\iint_S \boldsymbol{M}_S(t - \frac{r - \boldsymbol{r}'\cdot\hat{\boldsymbol{r}}}{c})dS'] \tag{9}$$

Where c is the speed of light in vacuum and η0 = (μ0/ϵ0)1/2. In addition, the Js = n×H and Ms = n×E terms are the electric and magnetic surface currents on the surface S, respectively, while n is the unit vector perpendicular to S. Therefore, the bistatic RCS at the far field direction (θ, φ) is computed by [16]

$$RCS(\theta,\varphi) = \lim_{r\to\infty}(4\pi r^2 \frac{P_{scat}}{P_{inc}}) \tag{10}$$

$$P_{scat} = \frac{1}{\eta_0}(\left|\dot{E}_\theta\right| + \left|\dot{E}_\varphi\right|) \tag{11}$$

Where Pinc is the power density of the incident electromagnetic wave and Pscat is the power density of scattering electromagnetic waves. The equations (6), (7) are used to calculate the RCS values of the SM objects.

3. Results and Discussion

The characteristics of incident and scattering fields are analyzed by simulation. The intensity and phase distribution of the incident field are shown in Fig 2. It presents that the radiation of OAM beam has a spiral wave front, which is different from plane wave in free space. The divergence angle and phase change period of radiogram are related to topological charge, and the phase uneven distribution is caused by calculation error.

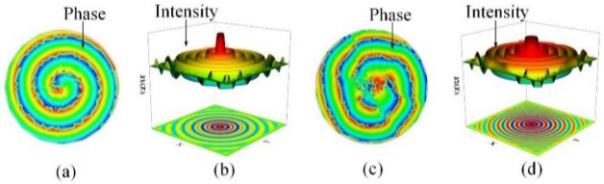

Fig. 2: Phase and intensity distributions of the incident electric field (y component). (a) Phase l=1; (b) Intensity l=1; (c) Phase l=2; (d) Intensity l=2.

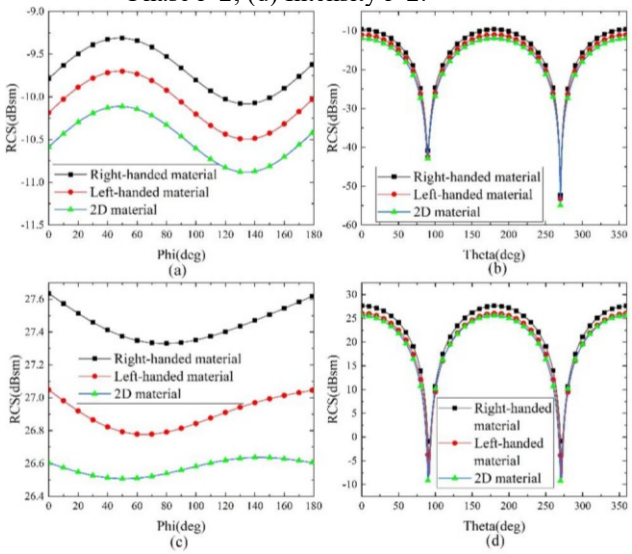

Fig. 3: The RCS values for cubes of three materials: (a) plane wave in the phi direction; (b) plane wave in the theta direction; (c) OAM wave in the phi direction; (d) OAM wave in the theta direction.

We use the RPIM and the empirical formula of the RCS to calculate the values of the RCS of the SM cube and the SM triangular pyramid. The SM target is excited with one order Bessel wave of bandwidth f = 10GHz, which is the X-band radar. For our time-domain simulations, a cubic cell with $\Delta x = \Delta y = \Delta z = 1 \times 10\text{-}2$m is selected, whereas the thickness of PML is 20 cells. Left-handed materials ($\varepsilon = -40$ and $\sigma = -3.9$ S/m) and two-dimensional materials MoS2 ($\varepsilon = 20.9907$ and $\sigma = 10$ S/m) are selected as stealth materials, and their RCS results are compared with right-handed materials ($\varepsilon = 40$ and $\sigma = 3.9$ S/m).

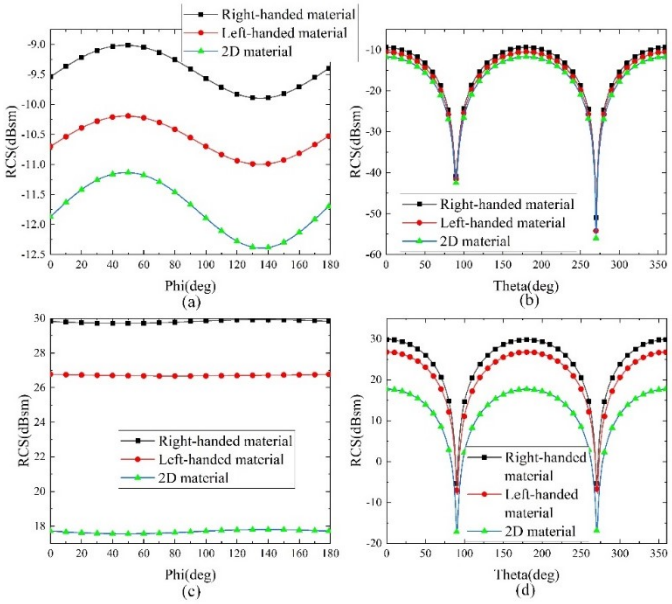

Fig. 4. The RCS values for triangular pyramid of three materials: (a) plane wave in the phi direction; (b) plane wave in the theta direction; (c) OAM wave in the phi direction; (b) OAM wave in the theta direction.

The RCS results are shown in Fig 3-4. Fig 3 and Fig 4 show the RCS values of cube and triangular pyramid of the right-handed, left-handed, two-dimensional MoS2 materials, respectively. There are the two directions of RCS, including the Phi angle in the Fig 3a and the Theta angle in the Fig 3b. Fig 3a and Fig 3b show that RCS of the cube illuminated by a plane wave. Fig 3c and Fig 3d show that RCS of the cube illuminated by an OAM wave. The results show that left-handed materials and two-dimensional materials can reduce the RCS of objects, especially in phi angle. However, the RCS of the target object increased significantly because of the OAM illumination. For the phi angle, the normal vector of the cone is constant. Thus, the constructive interference of the induced current at the surface of the SM triangular pyramid occurs at specific angles due to the identical amplitude and direction of the induced current.

The scattering of OAM beam on SM cube is studied. The schematic diagram of cube scattering is shown in Fig 1. The cube side length is set as 0.1m. Fig 5 describes the phase distribution of the scattered electric field (y component) in different OAM modes. And the OAM spectrum is shown in Fig 6. The results show that the scattering field still follows the spiral structure corresponding to the topological charge of the incident field, due to the conservation of axisymmetric angular momentum[13, 17]. Besides, a weak mixing of the OAM spectra occurs, which is mainly caused by the calculation error of the scattered field.

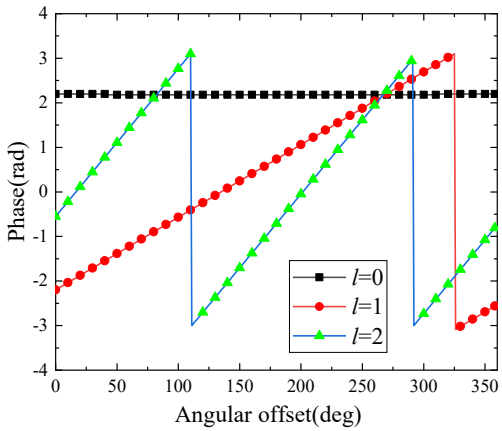

Fig. 5: The phase distribution of the scattered field from a SM cube with the side length of 0.1 m.

The scattering of SM triangular pyramid illuminated by OAM beam is studied, and the schematic diagram of cone scattering is shown in Fig 7. The bottom side length of equilateral triangular pyramid is set as 0.1m and the height is set as 0.2m. Fig 8 describes the phase distribution of the scattered electric field (y component) in different OAM modes, and the OAM spectrum is shown in Fig 9. The scattering field of SM triangular pyramid is also a vortex field.

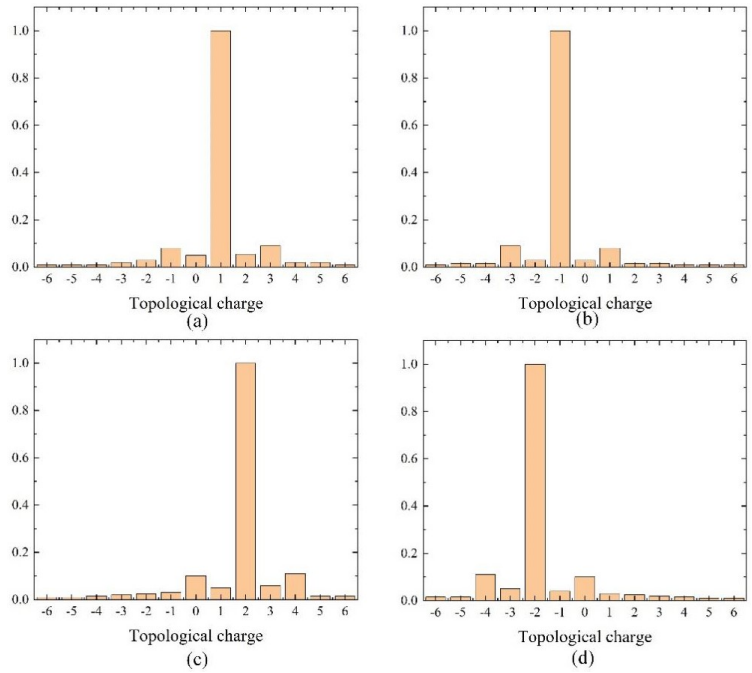

Fig. 6: The OAM spectra of the scattered field. (a) l=1; (b) l=-1; (c) l=2; (d) l=-2.

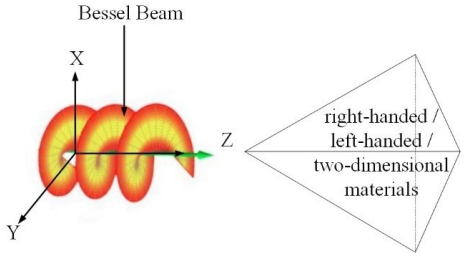

Fig. 7: The Schematic diagram of a stealth material triangular pyramid illuminated by Bessel vortex wave.

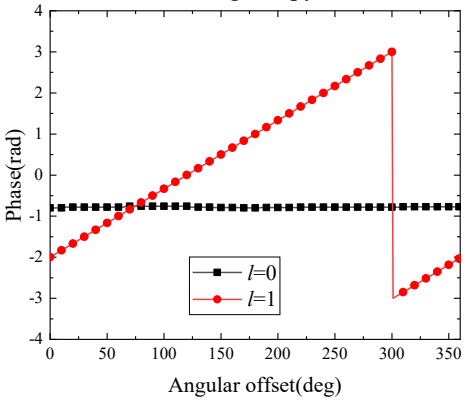

Fig. 8: The phase distribution of the scattered field from a SM triangular pyramid.

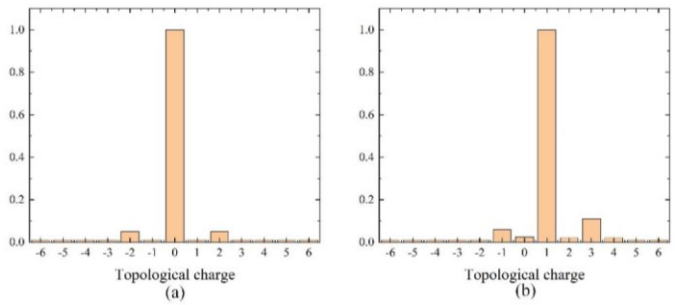

Fig. 9. OAM spectra of the triangular pyramid scattering field. (a) l=0; (b) l=1.

4. Conclusion

To conclude, the scattering characteristics of several typical stealth material objects illuminated by OAM wave are studied. The radial point interpolation method (RPIM) algorithm is used to calculate the electric and magnetic field values, and use the RCS empirical formula to calculate the value of the RCS. The RCS of stealth target irradiated by OAM wave and plane wave are compared. The results show that OAM wave can significantly increase the RCS of target object. Then, the scattering field of the target is analyzed, theoretical and simulation results indicated that the scattering field of OAM beam from axially symmetric objects is still vortex field when OAM beam is aligned to the symmetric axis. These results could be used as a reference for the study of scattering characteristics of vortex beam in OAM domain of stealth radar target.

5. References

[1] O. Tulgar, A. Arif Ergin. Improved Pencil Back-Projection Method with Image Segmentation for Far-Field/Near-Field SAR Imaging and RCS Extraction [J]. IEEE Transactions on Antennas and Propagation, 2015, 63(6): 2572-2584.

[2] Y. Liu, W. Hu, W. Zhang, et al. Radar Cross Section Near-Field to Far-Field Prediction for Isotropic-Point Scattering Target Based on Regression Estimation [J]. Sensors (Basel, Switzerland), 2020, 20(21).

[3] C. Hu, J. Xu, N. Li, et al. Signal processing techniques in high-resolution RCS measurement system[C]. proceedings of the 2009 4th IEEE Conference on Industrial Electronics and Applications, 2009.

[4] X. Fu, S. Peng, C. Zhang, et al. Normalized radar cross section measurement for space objects[C]. proceedings of the 2016 IEEE 11th Conference on Industrial Electronics and Applications (ICIEA), 2016.

[5] J. Li, Q. Zhang, G. Zheng. Research on Ultra-Wideband Radar Target Recognition Method[C]. proceedings of the 2020 2nd International Conference on Artificial Intelligence Technologies and Application, ICAITA 2020, August 21, 2020 - August 23, 2020, 2020.

[6] P.-C. Zhang, B.-Y. Li. Passive tracking and locating radar based on double GSM base stations[C]. proceedings of the Proceedings - International Conference on Electrical and Control Engineering, ICECE 2010, 2010.

[7] B. Ren, L. Shi, Y. Chang, et al. Polarization statistical properties of electromagnetic waves radiated from communication base stations to UHF band radar[C]. proceedings of the IET International Radar Conference 2015, October 14, 2015 - October 16, 2015, 2015.

[8] D. Orfeo, D. Huston, T. Xia. Study of OAM for Communication and Radar[C]. proceedings of the 2021 IEEE Radar Conference (RadarConf21), 2021.

[9] R. Li, C. Ding, K. F. Ren, et al. Scattering of a high-order Bessel beam by a sphere[C]. proceedings of the 2012 10th International Symposium on Antennas, Propagation and EM Theory, ISAPE 2012, October 22, 2012 - October 26, 2012, 2012.

[10] M. P. Yu, Y. Han, Z. Cui. Scattering of non-diffracting vortex electromagnetic wave by typical targets [J]. Progress in Electromagnetics Research Letters, 2017, 70: 139-146.

[11] Z. Wu, T. Qu, J. Wu, et al. Scattering of Electromagnetic Waves With Orbital Angular Momentum on Metallic Sphere [J]. IEEE Antennas Wirel Propag Lett, 2020, 19(8): 1365-1369.

[12] H. Liu, K. Liu, Y. Cheng, et al. Scattering Characteristics of Vortex Electromagnetic Waves by a Metal Plate[C]. proceedings of the 2020 9th Asia-Pacific Conference on Antennas and Propagation (APCAP), 2020.

[13] K. Liu, H. Y. Liu, W. E. I. Sha, et al. Backward Scattering of Electrically Large Standard Objects Illuminated by OAM Beams [J]. IEEE Antennas Wirel Propag Lett, 2020, 19(7): 1167-1171.

[14] A. Kumar, P. K. Ahluwalia. Tunable dielectric response of transition metals dichalcogenides MX2 (M=Mo, W; X=S, Se, Te): Effect of quantum confinement [J]. Physica B: Condensed Matter, 2012, 407(24): 4627-4634.

[15] A. Aoma, B. Bbk, A. Hr J Stacking impact on the optical and electronic properties of two-dimensional MoSe 2 /PtS 2 heterostructures formed by PtS 2 and MoSe 2 monolayers [J]. Chemical Physics, 532.

[16] C. Gao, Y. Jiang, J. Zhang, et al. Graphene-based wideband absorbing screen with radar cross section reduction[C]. proceedings of the International Symposium on Antennas, 2017.

[17] X. Xiong, A. Al-Jarro, L. J. Jiang, et al. Mixing of spin and orbital angular momenta via second-harmonic generation in plasmonic and dielectric chiral nanostructures [J]. Physrevb, 2017, 95(16): 165432.